A physics-based ignition model with detailed chemical kinetics for live fuel burning studies

Diba Behnoudfar[a], Kyle E. Niemeyer[a,*]

[a]*School of Mechanical, Industrial, and Manufacturing Engineering, Oregon State University, Corvallis, OR 97331, USA*

Abstract

This work presents a computationally inexpensive framework for modeling combined pyrolysis and gas-phase combustion of general vegetative fuels, which improves on existing solvers by incorporating detailed chemical kinetics and predicts the ignition behavior. The main motivation for this work is capturing the burning behavior of live wildland fuels, which can differ from those of dead fuels. Existing models are unable to accurately predict the ignition time and temperature variations for the live fuel cases. The kinetics model used here accounts for the non-primary constituents of fuels, or "extractives", which are expected to play a role in this distinct behavior. Validation studies show that the developed model is a promising tool for understanding the effects of fuel chemistry and spatial variation on ignition and fuel burning behavior. Case studies using the tool suggest that variations in ignition time can be explained by combined effects of variables such as moisture content, initial composition, and density.

Keywords: Wildland fire, live fuels, pyrolysis

*Corresponding author:
Email address: kyle.niemeyer@oregonstate.edu (Kyle E. Niemeyer)

Novelty and Significance Statement

We address a gap in the literature by developing a model that can simulate the pyrolysis and gaseous ignition of live wildland fuels. Existing methods that focus on pyrolysis and smoldering cannot capture the complex chemical kinetics of either pyrolysis or gas-phase combustion, and do not represent interactions between the solid and gas phases that lead to ignition. Similarly, existing detailed fluid dynamics models for fire behavior do not represent detailed gas-phase chemical kinetics, and do not typically couple with a pyrolysis model. We demonstrate the model's capability to predict pyrolysis products, temperatures, and ignition times for different plant species, accounting for subtle differences in composition. We examine relationships between fuel composition, moisture content, pyrolysis products, and ignition time.

Authors Contributions Statement

DB: developed model, performed computations, analyzed data, wrote manuscript
KEN: conceptualized research, provided critical feedback, edited manuscript

1. Introduction

Understanding the combustion behavior of multi-species, porous media is necessary for controlling many natural and engineered systems. Wildfire is a major environmental and societal concern that has become increasingly important in recent years due to climate change and the associated increase in

the extent of areas globally impacted by fires. In the field of energy production, optimizing biomass conversion reactors allows enhancing technologies for harnessing biofuels as a sustainable energy source [1] while controlling greenhouse gas emissions and air pollution; other examples include controlling heat shield burning of space vehicles [2] and thermal runaway in battery energy storage devices [3].

Ignition and combustion of wildland fuels have been extensively studied over the last 70 years, leading to models that describe fuel burning behavior with acceptable accuracy for dead fuels [4–7]. However, these models are unable to properly predict the behavior of living fuels [8]. Experiments based on the burning of live fuels show that they can sustain fire spread at higher moisture contents compared with dead fuels [8, 9]. These fires are often unpredictable and difficult to control. The chemical composition of live fuels differs from dead fuels in that, along with the main constituents (cellulose, hemicellulose, lignin, and water), they also contain sugars, lipids, proteins, phenols, and minerals [10]. These non-primary constituents are sometimes known as "extractives" in the literature [11]. The different burning behavior of living fuels has been mostly attributed to their high moisture content and different chemical composition. For example, Lamorlette et al. [12] found that the dynamics of moisture loss in live fuel are inconsistent with the assumption of equilibrium between solid and liquid phases in models. McAllister et al. [9] suggested that the chemical composition of live fuels should be included in the analysis to explain the variation in ignition behavior with seasonal changes.

Classical physical models for fuel burning behavior are mostly based on multiphase formulations [4–6, 13], which have been used as the basis for fire

simulators and solvers such as FireFOAM [14, 15], Fire Dynamics Simulator (FDS) [16], and Wildland-Urban Interface Fire Dynamics Simulator (WFDS) [6]. This approach basically considers the combustible medium as a distribution of solid particles (or fuel elements such as shrubs, twigs, and grass) and a gas that flows through them [4]. Solid particles are assumed to be motionless and thermally thin, meaning that the temperature throughout any particle is uniform at all times [7]. The approach includes separate but coupled models for solid and gas phases. The solid-phase model accounts for moisture evaporation followed by thermal degradation (pyrolysis), generally in the form of simplified one-step Arrhenius-like, temperature-dependent, mass-loss rates. The gas-phase model considers mass, momentum, and energy transfer using radiative and reactive Navier–Stokes equations with interface relationships to couple the solid and gas phases [7].

Other attempts use a more-complex framework for modeling solid-phase combustion to improve the predictive accuracy of models [17, 18]. For instance, GPyro [17, 19] provides the ability to solve three-dimensional heat, mass, and momentum transfer in the solid phase, unlike previous models (as in FireFOAM and WFDS) that divide the objects into multiple one-dimensional "patches." It can also incorporate multi-step complex reaction models, though with limitations on the number of species and reactions. GPryo has been successfully used to model pyrolysis and smoldering, for example in peat [20–24] and woody fuels [25, 26].

Most earlier chemical kinetics models for the combustion of wildland fuels represent the fuel as a combination of three main constituents—cellulose, hemicellulose, and lignin—and moisture in a over-simplified manner, ignoring

the non-primary constituents. Ranzi and Debiagi et al. [11, 27] recently proposed a multistep kinetic model to describe the pyrolysis of general types of biomass by characterizing composition in terms of a limited number of reference species including ones to represent extractives, i.e., triglyceride and tannin. The method well-predicts the thermogravimetric analysis (TGA) results for a wide range of biomass samples including wood plants (such as pine and almond trees) and grasses (such as switchgrass and wheat). The group further developed a complex framework for the pyrolysis of biomass particles to solve the transport equations at the pore level and for arbitrary geometries [28].

The above frameworks, while effective for solving pyrolysis and smoldering problems, are unable to handle the pyrolysis gases as they issue into the surrounding environment, necessary for ignition calculations. There have been reports of models for estimating the ignition time based on the assumption of pyrolysis time being equal to the ignition time [29]; however, these models oversimplify the problem, limiting it to certain conditions, and do not provide a way to investigate the effect of chemistry on gas-phase combustion. This work aims to fill in the gap by developing a physics-based solver for predicting the ignition time of live fuels using the above-mentioned detailed kinetics model for both solid and gas phases.

In this article, we first introduce a mathematical model of porous media ignition, discuss the pyrolysis and gas-phase domain combustion sub-models along with the numerical methods, and clarify all required material parameters. Second, we validate the model by comparing with experimental results for dead and live fuel combustion. Finally, we analyze the relationship be-

tween model variables and ignition characteristics, and lay the groundwork for future studies of live fuel burning.

2. Methods

The proposed ignition model uses a one-dimensional domain, combining

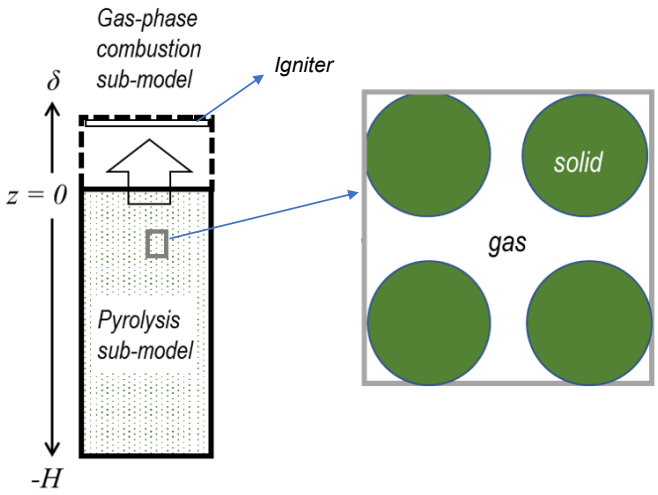

Figure 1: Schematic of computational domain, showing solid- and gas-phase sub-domains/sub-models.

2.1. Pyrolysis

The pyrolysis sub-model solves conservation of mass, species, and energy in a heterogeneous medium, considered to be a porous material, composed of separate solid and gas phases. To model the process, the conservation laws

are applied to each phase, though at a higher scale rather than at the pore level. This means that we assume the solid and gas are distributed uniformly in each control volume, which is permeable to gaseous mass transfer but impermeable to solid-phase mass transfer.

Solid phase. The governing equations expressing conservation of energy and mass for the solid phase [17] are

$$\frac{\partial}{\partial t}\left(\overline{\rho_s c_s} T\right) = \frac{\partial}{\partial z}\left(\overline{k_s}\frac{\partial T}{\partial z}\right) + \frac{\partial \dot{q}_r''}{\partial z} + \sum_{k=1}^{N_R} \dot{\omega}_k''' \Delta h_k \quad \text{and} \tag{1}$$

$$\frac{\partial}{\partial t}\left(\overline{\rho_s}\right) = -\sum_{j=1}^{N_S} \dot{\omega}_j''' \,, \tag{2}$$

where T is temperature; $\dot{\omega}_k'''$ and Δh_k denote the net rate and enthalpy of reaction k; $\dot{\omega}_j'''$ is the net production rate of gaseous species j; N_R and N_S are the numbers of reactions and species, respectively; q_r'' is the in-depth radiative heat flux; and $\overline{\rho_s}$, $\overline{c_s}$ and $\overline{k_s}$ are the mixture-averaged solid density, specific heat capacity, and conductivity, respectively, which are evaluated using weight- or volume-averaging methods:

$$\overline{\rho_s} = \frac{1-\phi}{\sum_{i=1}^{N_S} Y_i/\rho_i} \,, \tag{3}$$

$$\overline{c_s} = \sum_{i=1}^{N_S} c_i Y_i \,, \text{ and} \tag{4}$$

$$\overline{k_s} = \sum_{i=1}^{N_S} \frac{Y_i k_i/\rho_i}{\sum_{j=1}^{N_S} Y_j/\rho_j}(1-\phi) \,. \tag{5}$$

In the above equations, k_i and ρ_i are the conductivity and constant density of individual solid phase species, Y_i is the solid species mass fraction, and ϕ is porosity. Although this framework can incorporate detailed properties and

functional expressions, we use a simple model for estimating the individual heat capacity and thermal conductivity of solid species as Table 1 shows.

In Eq. (1), $\frac{\partial \dot{q}_r''}{\partial z}$ is the divergence of in-depth radiative heat flux [30]; this term is only relevant for semi-transparent or porous materials that absorb radiation at depth and is usually modeled using an attenuation coefficient (denoted as τ here):

$$\frac{\partial \dot{q}_r''}{\partial z} = -\tau \dot{q}_r'' \, . \tag{6}$$

Assuming radiation is only normal to the surface and neglecting the emission from interior parts of the solid, the above equation (for a constant τ) becomes

$$\frac{\partial \dot{q}_r''}{\partial z} = -\bar{\epsilon} \dot{q}_s'' \tau \exp\left(-\tau z\right) , \tag{7}$$

where $\dot{q}_s''$ is irradiation and $\bar{\epsilon}$ is the mixture-averaged emissivity as calculated using individual solid emissivities in Table 1 and

$$\bar{\epsilon} = \sum_{i=1}^{N_S} \frac{Y_i \epsilon_i / \rho_i}{\sum_{j=1}^{N_S} Y_j / \rho_j} (1 - \phi) \, . \tag{8}$$

Table 1: Solid individual heat capacity and emissivity.

Species	Heat capacity [kJ/(kg K)]	ϵ_i [-]	Reference
Biomass	$1.5 + 0.001T$[K]	0.757	[17, 31]
Char	$0.7 + 0.0035T$[K]	0.957	[17, 32]
Water	4.188	0.950	[17, 33]

For the chemical kinetics of pyrolysis, we used the detailed biomass combustion model of Debiagi et al. [11] with 46 species and 28 reactions. All

reactions in this model involve single reactants and oxidation is not considered (i.e., we do not aim to model smoldering here, though this is possible with our model). The volumetric destruction rate of solid phase reactant i in reaction A is

$$\dot{\omega}_i'''|_A = Z_A T^n \exp\left(\frac{E_A}{RT}\right) m_i''' \,, \tag{9}$$

where Z_A and E_A are pre-exponential factor and activation energy for reaction A and m_i''' is the local mass of solid phase reactant i per unit volume. The formation rates of all other solid/gaseous species involved in reaction A are related to $\dot{\omega}_i'''|_A$ via stoichiometry.

Gas phase. For the gas inside the porous medium (i.e., in the pores), conservation of mass and species are considered without solving the energy equation, assuming thermal equilibrium between the gaseous and solid phases[1]:

$$\frac{\partial}{\partial t}\left(\overline{\rho_g}\phi\right) + \frac{\partial}{\partial z}\left(\dot{m}''\right) = \sum \dot{\omega}_j''' \quad \text{and} \tag{10}$$

$$\frac{\partial}{\partial t}\left(\overline{\rho_g}\phi Y_j\right) + \frac{\partial}{\partial z}\left(\dot{m}'' Y_j\right) = \frac{\partial}{\partial z}\left(\overline{\rho_g}\phi D \frac{\partial Y_j}{\partial z}\right) + \dot{\omega}_j''' \,, \tag{11}$$

where $\overline{\rho_g}$ is the gas density, Y_j is gas phase species mass fraction, $\dot{m}''$ is mass flux, and D is the effective binary diffusion coefficient assuming that all gaseous species have the same diffusivity as oxygen diffusing into the nitrogen environment. This assumption is made to simplify the calculations, but as stated before the framework can handle more-detailed properties. Since the porous medium is permeable to gaseous mass transfer, Fick's law describes

[1] According to Mulky and Niemeyer [25], making this thermal-equilibrium assumption in simulations of smoldering in porous media changes the calculated propagation speeds by just 5.6%.

the species' diffusive fluxes. The binary diffusion coefficient for species A diffusing into species B is (based on Chapman–Enskog theory):

$$D_{AB} = 0.018829 \frac{\sqrt{T^3 \left(\frac{1}{M_A} + \frac{1}{M_B}\right)}}{P \sigma_{AB}^2 \Omega_{D,AB}} \,, \tag{12}$$

where M_A and M_B are molecular weights, T is temperature, P is pressure, and σ_{AB} and $\Omega_{D,AB}$ are model parameters tabulated for some gases by Bird et al. [34]. The convective mass transfer is considered using Darcy's law to express the momentum balance:

$$\dot{m}'' = -\frac{K}{\nu} \left(\frac{\partial P}{\partial z}\right) \tag{13}$$

$$P = \frac{\overline{\rho_g}}{M} RT \,, \tag{14}$$

where K is permeability, ν is kinematic viscosity, and M denotes average molecular weight. Using the unity Schmidt and Lewis numbers assumption, viscosity is approximated as $\nu \approx D$. As seen in Eq. (14), the ideal gas assumption is used to evaluate pressure.

2.2. Gas-phase combustion

A simplified gas-phase combustion sub-model solves the energy and species conservation equations for the pyrolyzates as they issue into the surrounding air. This model assumes laminar, constant-density combustion with negligible kinetic energy and pressure changes; hence, the velocity field is uniform but varies with time:

$$\frac{\partial}{\partial t}\left(\rho c_p T\right) + \dot{m}'' \frac{\partial}{\partial z}\left(c_p T\right) = \frac{\partial}{\partial x}\left(\rho D c_p \frac{\partial T}{\partial x}\right) - \sum \dot{\omega}_j''' h_j \text{ and} \tag{15}$$

$$\frac{\partial}{\partial t}\left(\rho Y_j\right) + \dot{m}'' \frac{\partial Y_j}{\partial z} = \frac{\partial}{\partial x}\left(\rho D \frac{\partial Y_j}{\partial x}\right) + \dot{\omega}_j''' \,, \tag{16}$$

where h_j denotes enthalpy of individual gas species. The energy equation given in Eq. (15) is expressed in Shvab–Zeldovich form [35], assuming no viscous dissipation, no radiation heat transfer, unity Lewis number (Le $= k/\rho c_p D$), and no diffusion in the flow direction. The model only solves gas-phase combustion up to the point of ignition and not beyond; we are not attempting to simulate flame propagation. The sub-model is linked to pyrolysis through the boundary conditions as explained in the next section.

The gas-phase chemical kinetic model is again based on the detailed biomass combustion model from Ranzi et al. [27] with 137 species and 4533 reactions for gas-phase combustion (`bio1412` from the CRECK modeling group).

2.3. Boundary conditions

This section describes the boundary condition used for simulating the cone calorimetry experiments discussed in Section 3.1. The ignition model discussed here is not designed to work with forced air convection, which would undermine the assumptions discussed in Section 2.2. For cases with radiative heating on the top of the sample, the heat flux at the top boundary in the pyrolysis sub-model is (for $\tau \to \infty$)

$$\left(-\overline{k}_s \frac{\partial T}{\partial z}\right)\bigg|_{z=0} = \bar{\epsilon}\dot{q}_s{}'' - h(T - T_\infty) - \bar{\epsilon}\sigma(T^4 - T_\infty^4) \tag{17}$$

and for non-opaque materials ($\tau \neq \infty$) the heat flux is

$$\left(-\overline{k}_s \frac{\partial T}{\partial z}\right)\bigg|_{z=0} = \bar{\epsilon}\dot{q}_s''(1-\tau) - h(T - T_\infty) - \bar{\epsilon}\sigma(T^4 - T_\infty^4)\ , \tag{18}$$

where h denotes convective heat transfer coefficient, q_s'' is irradiation, $\bar{\epsilon}$ is the mixture-averaged emissivity given by Eq. (8), and T_∞ is the ambient temperature.

At the top boundary, the pressure is atmospheric and gas diffusion is approximated as

$$\left(-\overline{\rho_g}\phi D\frac{\partial Y_j}{\partial z}\right)\Bigg|_{z=0} \approx h_m\left(Y_j^{\infty} - Y_j\big|_{z=0}\right) \ , \tag{19}$$

where h_m is the diffusive mass transfer coefficient. The bottom face and the sides of the solid domain are assumed impermeable and insulated so there is no mass and heat flux across the bottom face:

$$\left(-\overline{k_s}\frac{\partial T}{\partial z}\right)\Bigg|_{z=-H} = 0 \ , \tag{20}$$

$$\left(-\overline{\rho_g}\phi D\frac{\partial Y_j}{\partial z}\right)\Bigg|_{z=-H} = 0 \text{ , and} \tag{21}$$

$$\dot{m}''\big|_{z=-H} = 0 \ . \tag{22}$$

For the gas-phase combustion sub-model, time series of temperature, mass flux, and mass fraction are provided at the inlet boundary (at the interface with the solid):

$$T\big|_{z=0} = T_{in}(t) \ ,$$
$$\dot{m}''\big|_{z=0} = J_{\text{in}}(t) \ , \text{ and}$$
$$Y_j\big|_{z=0} = Y_{\text{in}}(t,j) \ .$$

At the side boundaries, the ambient (stagnant) air condition applies and the pressure is atmospheric in the entire domain. For cases with an igniter, the temperature at the top boundary ($z = \delta$) is set to an initial temperature and is only allowed to change by the heat release from the reactions:

$$T(t=0)\big|_{z=\delta} = T_i \text{ and} \tag{23}$$

$$\frac{\partial}{\partial t}\left(\rho c_p T\right)\Bigg|_{z=\delta} = -\sum \dot{\omega}_j''' h_j \ . \tag{24}$$

2.4. Numerical methods

The pyrolysis and gas-phase combustion sub-models are solved separately in a decoupled fashion, linked through the boundary conditions. The above-mentioned partial differential equations are spatially discretized using the finite volume method with upwind differencing for advective terms and piece-wise linear approximation for diffusive fluxes. The Supplementary Material presents the discretized form of these equations. The resulting ordinary differential equations (ODEs) are time integrated using a variable-step, variable-order (VSVO) solver based on the numerical differentiation formulas of orders one to five [36].

For the gas-phase combustion sub-model, we use an operator-splitting technique to accelerate the solution process and avoid numerical difficulties due to the coupling of chemical kinetics and fluid flow. Operator-splitting methods divide the time integration into several sub-steps, separating the reaction part from the transport one at each time step [37, 38]. In the Strang splitting method adopted here (which is second-order accurate) [39], the transport part is first integrated over half of the time step, $\Delta t/2$. Next, the chemical source term is integrated over the original time step, Δt. Last, the transport part is again integrated over the remaining $\Delta t/2$.

To implement the solution process, we use MATLAB's `ode113` solver [36] with ODE functions defined to compute the right-hand side of the differential equations. The reaction rates and thermodynamic properties (for the gas phase) are evaluated using Cantera [40], an open-source software tool for systems involving complex chemical kinetics and the associated thermodynamics and transport properties. The Supplementary Material provides

an example pseudocode to demonstrate the algorithmic workflow, and the software implementation is available openly [41].

3. Results and discussion

In this section, we first use the proposed model to simulate two experiments available in the literature: non-charring gasification of white pine [42] and piloted ignition of Eucalyptus saligna leaves [43], to examine the performance of the model on both dead and live fuels. We then explore the relationships between model variables, leveraging the detailed chemical kinetics.

3.1. Model evaluation

In the first set of experiments, a pine cube is irradiated in a nitrogen environment [42]. The sample is considered dead fuel. This experiment has been previously simulated with the software Gpyro [17], considering six solid-phase species and a two-step reaction model. In the second experiment, a biomass bed comprising live Eucalyptus leaves with a range of moisture contents is irradiated in open air. Table 2 summarizes the experimental conditions and model parameters.

Figure 2 compares model calculations and the experimental temperature measurements for white pine gasification. The solver slightly over-predicts temperature at 10 mm, but the calculated temperatures at the surface and 5 mm match the experimental data closely. Figure 3 shows the calculated and experimental mass fractions of pyrolysis gases at the surface of the sample, demonstrating the capability of the model in predicting the detailed composition of pyrolyzates. The experimental data on the evolution of water

Table 2: Operating conditions of experiments. Species names include short names from source kinetic model.

Properties	Experiment 1	Experiment 2
Material	White pine	Eucalyptus saligna leaves
Shape	cube	biomass bed
Dimension	3.8 cm	10 cm × 10 cm × 2.8 cm
Initial density [kg/m^3]	380	30
Moisture content [%]	5	25–119
Irradiance ($\dot{q}''_s$) [kW/m^2]	25 or 40	50
Permeability (K) [m^2]	1×10^{-10} [17]	1×10^{-7}
Diffusive coefficient (h_m) [kg/m^2/s]	0.01 [17]	0.01
Convective coefficient (h) [W/m^2/K]	10 [17]	10
Attenuation coefficient (τ) [-]	∞	0.15 [44]
Composition (% weight)		
cellulose (CELL)	0.4254	0.4571
hemicellulose (HCELL)	0.1927	0.1725
H-rich lignin (LIGH)	0.0998	0.0186
O-rich lignin (LIGO)	0.0482	0.1861
C-rich lignin (LIGC)	0.1658	0.0692
triglyceride (TGL)	0.0326	0.0121
tannin (CTANN)	0.0354	0.0844

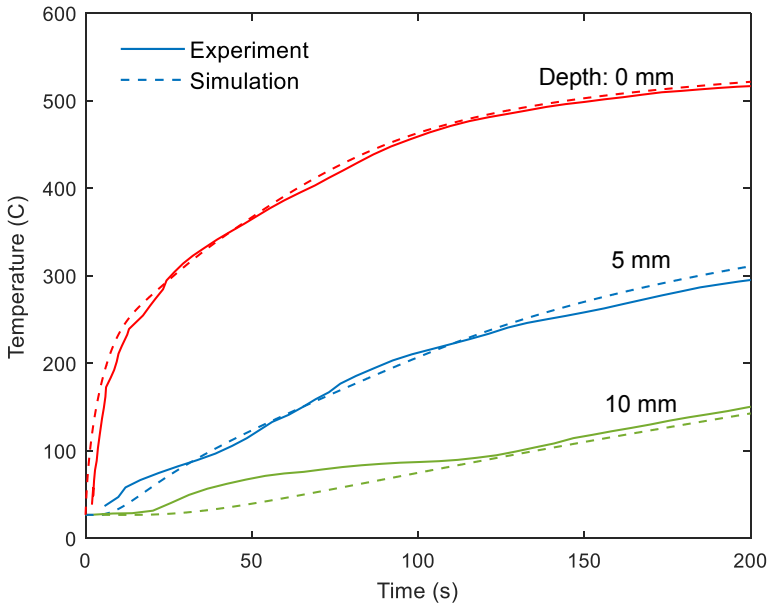

Figure 2: Temperature profiles at different depths of white pine pyrolysis for $40\,\mathrm{kW/m^2}$ heat flux experiment.

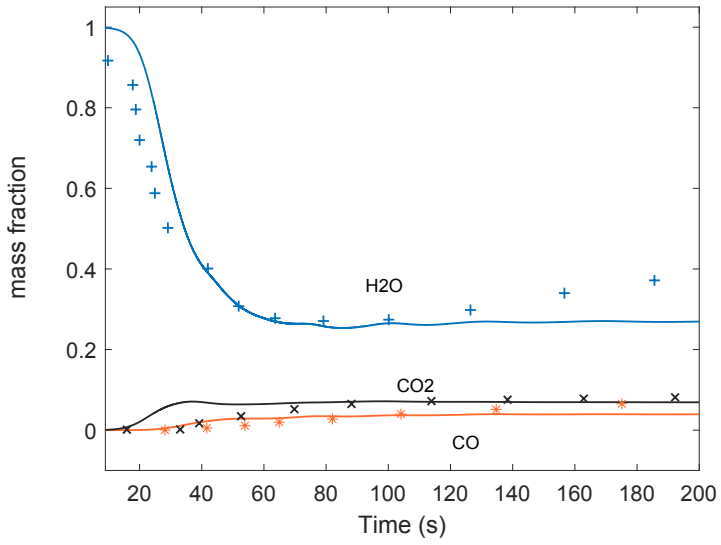

Figure 3: Comparison of calculated mass fraction and experimental data of select major species in the pyrolysis products for $40\,\mathrm{kW/m^2}$ heat flux experiment of white pine. Solid lines denote simulation data and the markers represent experimental data.

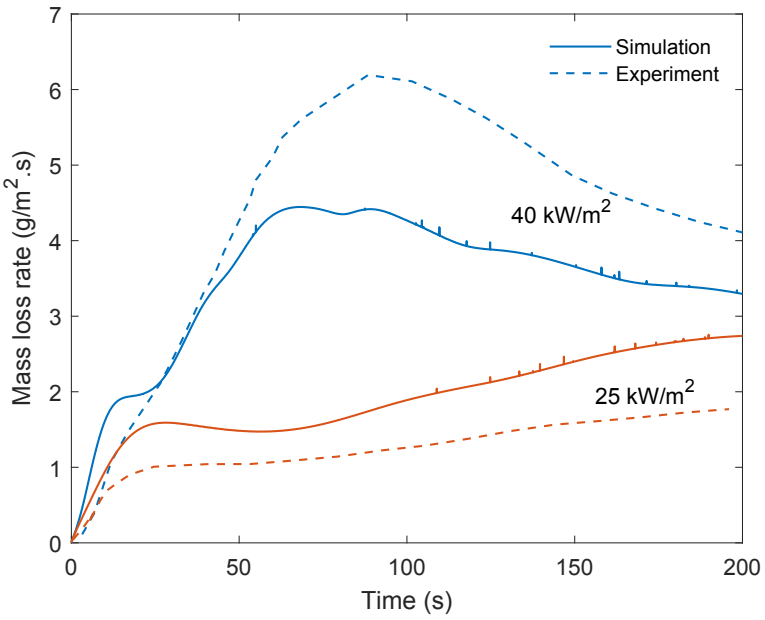

Figure 4: Comparison of calculated mass loss rate and experimental data for pyrolysis of white pine at 25 and 40 $\mathrm{kW/m^2}$ heat fluxes.

are qualitatively valid but quantitatively inaccurate due to some measuring probe calibration issues [42].

Figure 4 shows the predicted mass loss rates for heat fluxes of 25 and 40 kW/m^2. Although the results are acceptable for the lower heat flux and the shape of the curves match well with the experiment for both cases, our model underpredicts peak mass loss rate, and it occurs ∼15 s earlier than in the 40 kW/m^2 heat flux experiment. This discrepancy can be partly attributed to the inaccuracies in estimating the initial sample composition used in the model. The CRECK Biomass Database [11], from which the sample composition is derived, only contains one datapoint for eastern white pine, while Kashiwagi et al. [42] do not specify the exact variety of the white pine wood used in their experiments. It is possible that the model underrepresents certain components with higher decomposition rates at higher temperatures (see Figure 14).

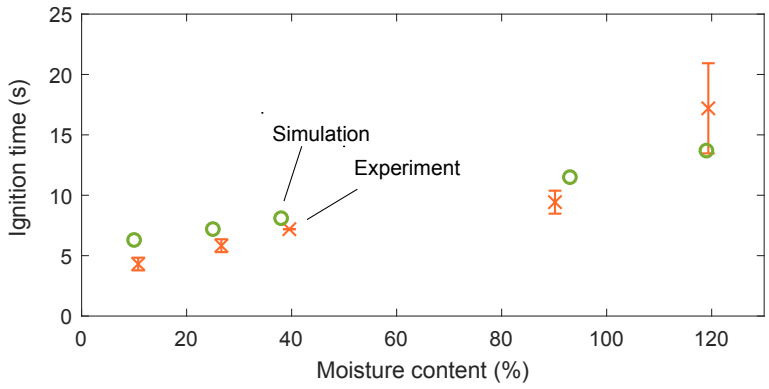

Figure 5: Ignition time for live Eucalyptus leaves for varying moisture content. The error bars indicate the standard deviation in the experimental measurements.

Looking at the second set of experiments, Figure 5 shows the simulated

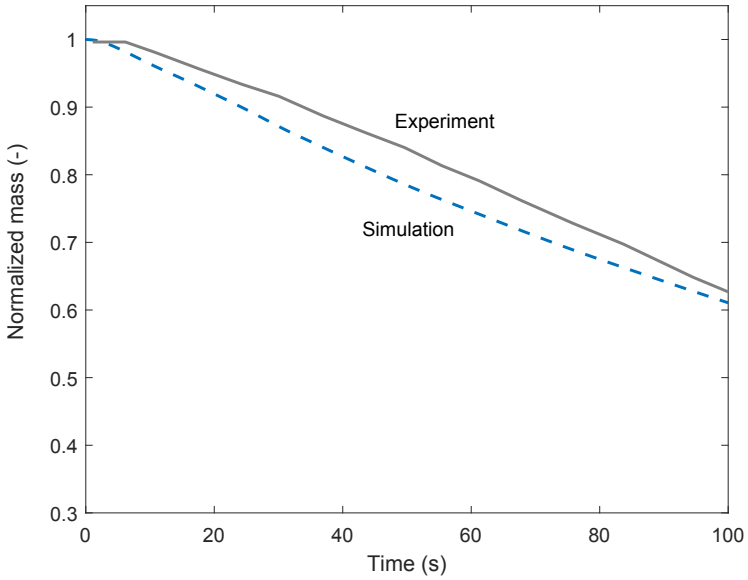

Figure 6: Mass loss evolution for live Eucalyptus leaves with 114% moisture content at $50\,\mathrm{kW/m^2}$ heat flux.

ignition times for live Eucalyptus leaves and the associated experimental values. The model correctly predicts the trends with varying moisture content, and in most cases, the calculated ignition time is within 10–30% of experimental data or within the error range. Figure 6 shows an instance of the mass loss evolution calculations. The agreement with the experimental data is acceptable considering the uncertainty associated with the experiment and the estimation of the medium's in-depth radiative heat transfer properties. It would be possible to better tailor chemical composition and/or heat transfer parameters to better fit the experimental data, but this is beyond the scope of our work here.

3.2. Relationship between the initial composition, pyrolysis products, and ignition delay time

In the Eucalyptus leaves ignition experiments of Ramadhan et al. [43], a higher moisture content seems correlated to an increase in the ignition delay time, as Figure 5 shows. To explain this effect (and in general the effect of initial composition) on the variables of interest, we take a deeper look at how the model variables are interconnected. Starting from the gas-phase combustion, we backtrack the chain of processes that lead to ignition. Assuming an elementary homogeneous reaction and an initially high temperature (in the presence of an igniter), the reaction rate is controlled by the concentration of reactants. A reaction heat release analysis at the time of ignition reveals that the following reactions most significantly drive the fast heat-releasing

combustion:

$$HO_2 + OH \rightleftharpoons H_2O + O_2$$

$$H + O_2 + M \rightleftharpoons HO_2 + M$$

$$CO + OH \rightleftharpoons CO_2 + H$$

$$HCO + O_2 \rightleftharpoons CO + HO_2$$

$$CH_2O + OH \longrightarrow H_2O + HCO$$

The above reactions play important roles in hydrocarbon combustion [35]; in general, the fuel molecule (here, the pyrolysis products) is attacked by O and H radicals and breaks down, primarily forming smaller olefins (such as C_2H_4) and hydrogen; hydrogen oxidizes to water; olefins further oxidize to CO and H_2; and finally CO oxidizes to CO_2.

Continuing to work backwards, Figure 7 shows a reaction path analysis following elemental hydrogen and carbon, performed at the time of ignition in the Eucalyptus leaf experiment at 93% moisture content and produced using Cantera's reaction path analyzer [40]. The starting fuel compounds leading to the formation of the radicals/reactants in the above reactions are ethylene (C_2H_4) and methane (CH_4). Ethylene is mainly produced by the decomposition of pyrolysis products hydroxymethylfurfural ($C_6H_6O_3$), propanal (C_2H_5CHO), and coumaryl ($C_9H_{10}O_2$) and is also a direct pyrolysis product. Similarly, methane, formaldehyde (CH_2O), and carbon monoxide (CO) are produced both during the pyrolysis and gas-phase combustion. Figures 8 and 9 show the mass fraction evolution of major fuels and radicals produced during gas-phase combustion and pyrolysis, respectively. The concentrations of these fuels determine the reaction rates and consequently

the ignition time. Figure 8 illustrates this, where the rise in mass fractions of fuels (C_2H_4 and CO) coincides with the sharp increase in temperature and drop in the oxidizer fraction. Based on species conservation (given in Eq. (16)), these concentrations are controlled by total mass flux of the pyrolysis products leaving the solid surface ($\dot{m}''$) and their mass fractions (Y_j) at that location. Figure 9 demonstrates how the increase in moisture content delays the formation of major fuels during pyrolysis at the solid surface.

Following the chain of processes to the solid phase, the graph in Figure 10 summarizes the variables in the pyrolysis sub-model and their dependencies. Temperature plays a central role, connecting most of the variables. The solid composition (Y_j) and temperature determine the rates of destruction/production of solid ($\dot{\omega}_i'''$) and gas species ($\dot{\omega}_j'''$) based on Eq. (9). Temperature, on the other hand, is a function of net heat release rate of reactions ($\sum \dot{\omega}_k''' \Delta h_k$), irradiation ($q_s''$), convective coefficient (h), and physical properties (Eq. (1)), which themselves depend on solid composition (Y_i) through Eqs. (3)–(5). The transport part of the model and consequently the total mass flux ($\dot{m}''$) is also governed by temperature, since it determines the pressure gradients (Eqs. (15)–(16)).

We now return to the main question of why increasing the moisture content delays the production of fuels in the pyrolysis gases. Given the central role of temperature, the most straightforward way to answer this is by looking at the variations of variables controlling the temperature. Figure 11 shows the result of this analysis for a fixed heat flux and convective heat transfer coefficient. Among the variables analyzed, the solid density and net heat release rate significantly change with increasing the moisture content. As ex-

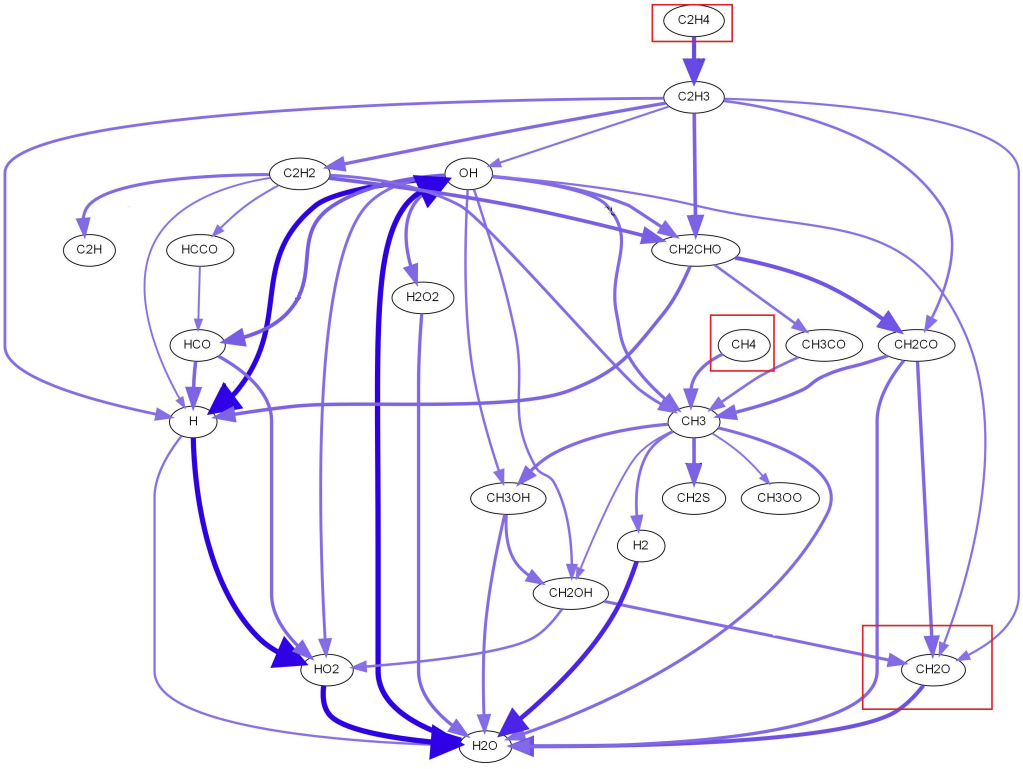

Figure 7: Major reaction pathways following the hydrogen element at the time of ignition for the Eucalyptus leaves experiment with 93% moisture content. The thickness of the arrows represents the flux between two species and the boxed species are the major fuels leading to the formation of radicals/reactants in the fast heat-releasing combustion reactions.

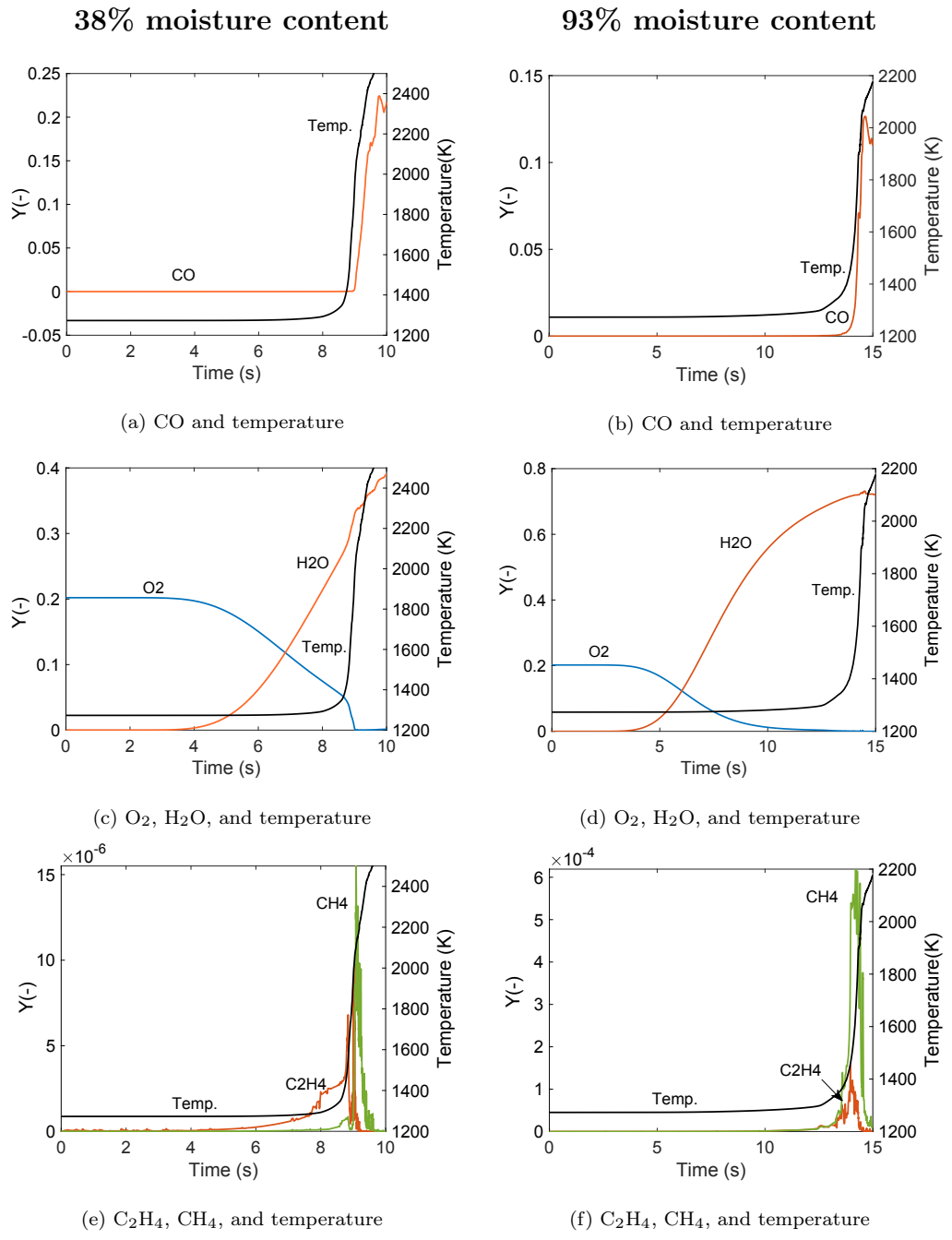

(a) CO and temperature

(b) CO and temperature

(c) O_2, H_2O, and temperature

(d) O_2, H_2O, and temperature

(e) C_2H_4, CH_4, and temperature

(f) C_2H_4, CH_4, and temperature

Figure 8: Mass fractions of major fuels and temperature versus time for gas-phase combustion of Eucalyptus leaves at the location of the igniter.

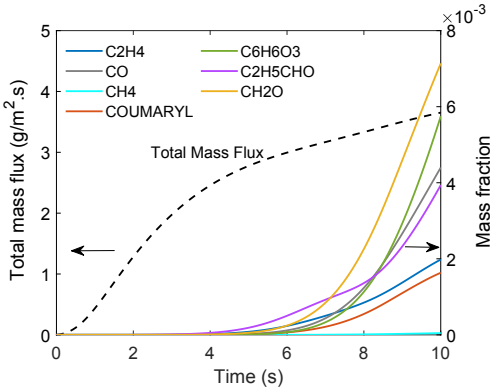

(a) 38% moisture content

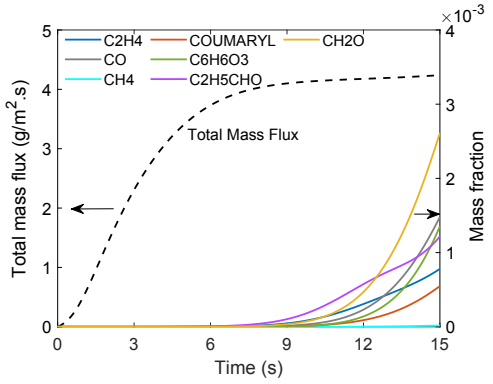

(b) 93% moisture content

Figure 9: Mass fractions of major fuels and total flux for pyrolysis of Eucalyptus leaves at the surface of the solid.

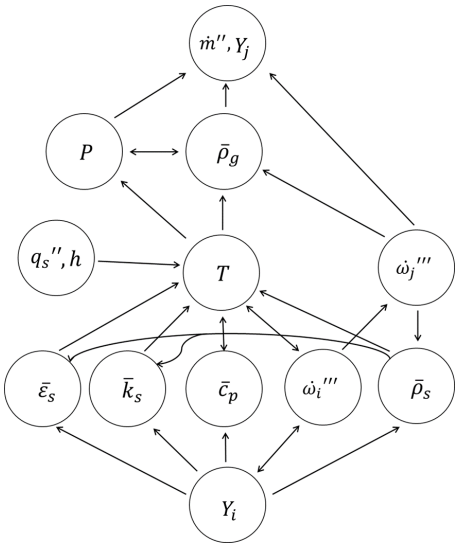

Figure 10: Dependency graph for variables involved in pyrolysis sub-model.

pected, a sample with more water should absorb more heat since vaporization is an endothermic process; a higher moisture content also increases the solid density, which is inversely proportional to temperature (Eq. (1)). The combination of these two effects decreases the rate of temperature growth and eventually delays the production of gaseous fuels during pyrolysis. Other studies focused on smoldering combustion reported similar trends: increasing the fuel's moisture content and density reduces smoldering propagation rate and peak temperature [24, 26].

3.3. An ignition study of various plant species

To demonstrate the solver's usefulness for investigating the effect of fuel chemistry on ignition, we selected six plant species with well-validated compositions [11] and calculated their ignition delay times. Table 3 and Figure 12 show the initial composition of these species, and Figure 13 shows the corre-

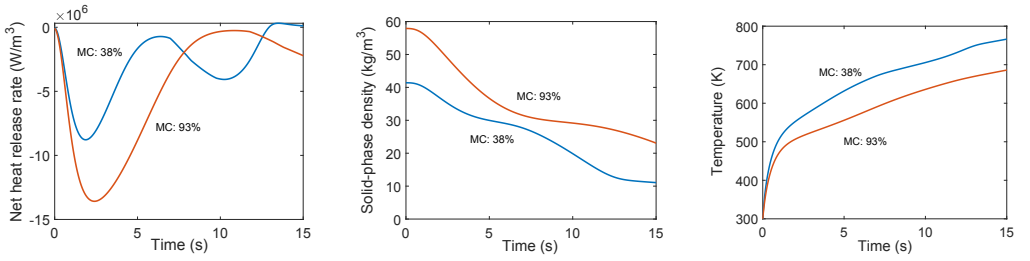

(a) Net heat release rate (b) Solid density (c) Temperature at solid surface

Figure 11: Effect of moisture content on model variables for Eucalyptus leaves pyrolysis with 38% and 93% moisture contents.

sponding ignition times. Overall, the grasses and needles (switch grass, wheat straw, and pine needle) take longer to ignite compared with the wood-like plants (almond chips, almond hulls, and pine bark).

One interesting outcome is the noticeable difference between the ignition times of two different organs of the same plant: pine bark and pine needles. This has implications for fire initiation location and spread direction. For example, if the fuel composition controls ignition in a particular case of pine tree burning, one can make rough predictions about which parts of the tree ignite faster. Such a question has not been studied extensively before, although there have been observations that most unpredictable fires often occur in crowns of vegetation, with higher spread rate [9, 45].

The differences in ignition times between pine bark and pine needles can be explained by looking at the Derivative Thermogravimetry (DTG) analysis of each fuel component (Figure 14). Comparing the initial compositions of the two samples, pine needles have higher cellulose and triglyceride contents, which require higher temperatures (and thus more time) to decompose. According to Figure 14, the higher ignition time of wheat straw probably results

Table 3: Initial composition (weight fractions) of select plant species; see Table 2 for the explanation of the components' names [11].

Component	almond chips	almond hull	switchgrass	wheat straw	pine bark	pine needle
CELL	0.4571	0.4386	0.4748	0.4009	0.3911	0.5859
HCELL	0.1752	0.2257	0.3658	0.3012	0.1657	0.2571
LIGH	0.0186	0.0888	0.0030	0.0249	0.1076	0.0458
LIGO	0.1861	0.1366	0.0982	0.1623		0.0002
LIGC	0.0652	0.0202	0.0015	0.0008	0.2573	0.0068
TGL	0.0121	0.0430	0.0238	0.0146	0.0222	0.1042
CTANN	0.0844	0.0471	0.0330	0.0952	0.0562	
H2O	0.0500	0.0500	0.0500	0.0500	0.0500	0.0500

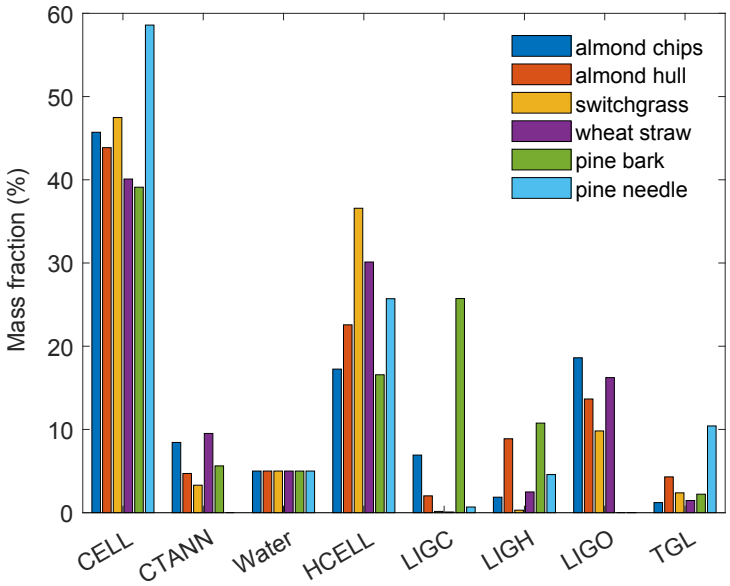

Figure 12: Initial composition of plant species described in Table 3, with components cellulose (CELL), hemicellulose (HECELL), H-rich lignin (LIGH), O-rich lignin (LIGO), C-rich lignin (LIGC), triglyceride (TGL), and tannin (CTANN).

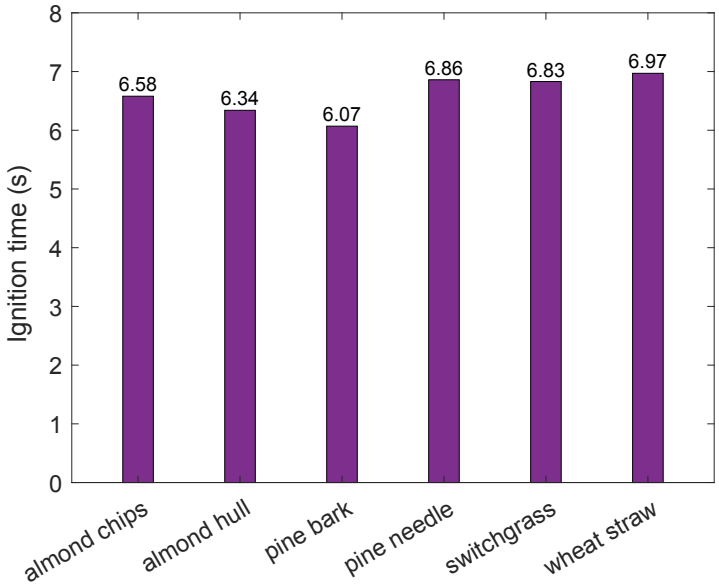

Figure 13: Calculated ignition times of select plant species.

from its larger content of O-rich lignin with a higher activation temperature, as opposed to the high C-rich lignin content in pine bark that reacts at lower temperatures.

4. Conclusion

In this study, we developed a one-dimensional ignition model based on physical laws and using detailed chemical kinetics that applies to a wide range of plant species by modifying the initial composition of the reference components. This eliminates the need for empirical correlations or fitting parameters that are commonly used in similar studies. We validated this model against measurements of mass loss, temperature, and ignition time in both pyrolysis and combustion experiments, showing overall good agreement

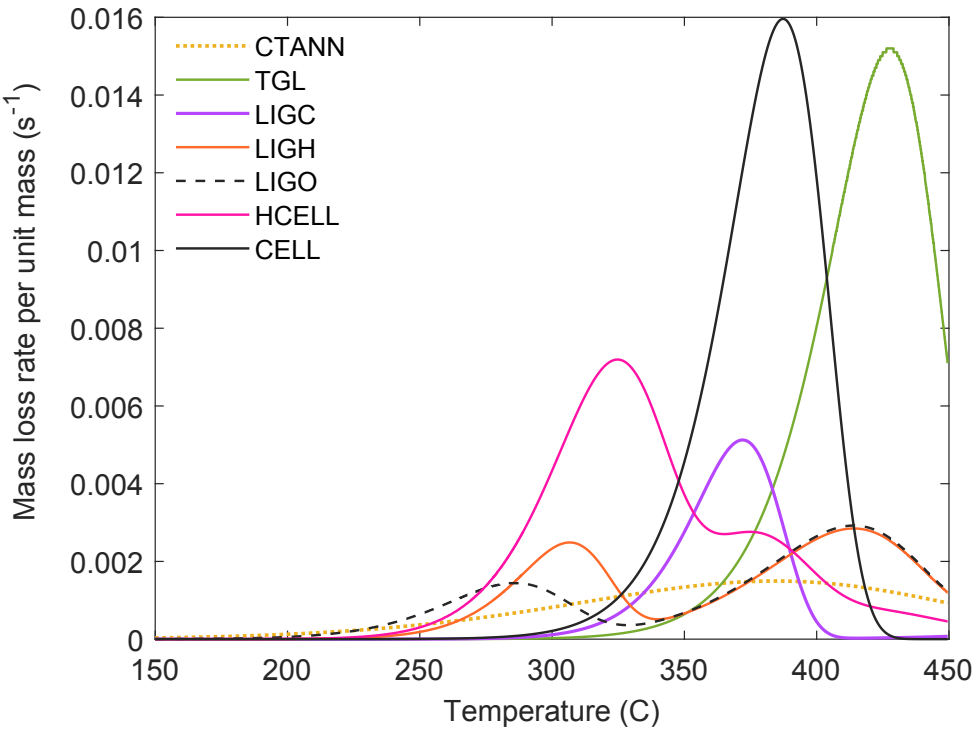

Figure 14: DTG analysis of each fuel component, including cellulose (CELL), hemicellulose (HECELL), H-rich lignin (LIGH), O-rich lignin (LIGO), C-rich lignin (LIGC), triglyceride (TGL), and tannin (CTANN).

despite the uncertainty in definitions of thermal and physical parameters. The detailed model developed in this work enhances the existing modeling tools (in the space of pyrolysis solvers) by adding a sub-model for solving the transport equations of pyrolysis gases as they issue into the surrounding environment and removing the limit for the number of allowed reactions, while remaining computationally inexpensive. Using this tool, we show that there exists a complex interplay between the solid properties, the pyrolysis rates, released products, and ignition time. In the context of live fuel burning studies, the model can be used to investigate the effect of initial composition and moisture content on the ignition time and fire initiation location. An ignition study of various plant species revealed that the ignition time can vary across different parts of the same plant—which was the case for the bark and needle parts of the pine tree.

Future work should extend the capability of model to handle different boundary conditions. The model currently supports radiative heating without air convection. Using such an extended model one can answer questions: does the fire start from the tree bark/branches and spread up to the foliage and the tree crown (given favorable conditions and a dry season)? Or, which of the small shrubs/grasses or trees are more fire-resistant?

Acknowledgments

This project was funded in part by a contract from the Strategic Environmental Research and Development Program (SERDP), project number RC19-1092. This material is also based upon work supported by the National Science Foundation under Grant No. 1931592.

Appendix A. Availability of material

The figures in this article, as well as the data and plotting scripts necessary to reproduce them, are available openly under the CC-BY license [46]. The software implementation of the model is available via GitHub under the MIT license, and the version used here is archived via Zenodo [41].

References

[1] M. Sharifzadeh, M. Sadeqzadeh, M. Guo, T. N. Borhani, N. M. Konda, M. C. Garcia, L. Wang, J. Hallett, N. Shah, The multi-scale challenges of biomass fast pyrolysis and bio-oil upgrading: Review of the state of art and future research directions, Prog. Energ. Combust. Sci. 71 (2019) 1–80.

[2] A. Harpale, S. Sawant, R. Kumar, D. Levin, H. B. Chew, Ablative thermal protection systems: Pyrolysis modeling by scale-bridging molecular dynamics, Carbon 130 (2018) 315–324.

[3] T. Cai, A. G. Stefanopoulou, J. B. Siegel, Modeling Li-ion battery temperature and expansion force during the early stages of thermal runaway triggered by internal shorts, J. Electrochem. Soc. 166 (2019) A2431.

[4] M. Larini, F. Giroud, B. Porterie, J.-C. Loraud, A multiphase formulation for fire propagation in heterogeneous combustible media, Int. J. Heat Mass Tran. 41 (1998) 881–897.

[5] D. Morvan, J.-L. Dupuy, Modeling of fire spread through a forest fuel

bed using a multiphase formulation, Combust. Flame 127 (2001) 1981–1994.

[6] W. Mell, A. Maranghides, R. McDermott, S. L. Manzello, Numerical simulation and experiments of burning douglas fir trees, Combust. Flame 156 (2009) 2023–2041.

[7] M. El Houssami, J. Thomas, A. Lamorlette, D. Morvan, M. Chaos, R. Hadden, A. Simeoni, Experimental and numerical studies characterizing the burning dynamics of wildland fuels, Combust. Flame 168 (2016) 113–126.

[8] B. M. Pickett, C. Isackson, R. Wunder, T. H. Fletcher, B. W. Butler, D. R. Weise, Experimental measurements during combustion of moist individual foliage samples, Int. J. Wildland Fire 19 (2010) 153–162.

[9] S. McAllister, I. Grenfell, A. Hadlow, W. Jolly, M. Finney, J. Cohen, Piloted ignition of live forest fuels, Fire Safety J. 51 (2012) 133–142.

[10] F. J. Matt, M. A. Dietenberger, D. R. Weise, Summative and ultimate analysis of live leaves from southern US forest plants for use in fire modeling, Energ. Fuel. 34 (2020) 4703–4720.

[11] P. E. A. Debiagi, C. Pecchi, G. Gentile, A. Frassoldati, A. Cuoci, T. Faravelli, E. Ranzi, Extractives extend the applicability of multistep kinetic scheme of biomass pyrolysis, Energ. Fuel. 29 (2015) 6544–6555.

[12] A. Lamorlette, M. El Houssami, D. Morvan, An improved non-equilibrium model for the ignition of living fuel, Int. J. Wildland Fire 27 (2018) 29–41.

[13] O. Séro-Guillaume, J. Margerit, Modelling forest fires. Part I: a complete set of equations derived by extended irreversible thermodynamics, Int. J. Heat Mass Tran. 45 (2002) 1705–1722.

[14] Y. Wang, P. Chatterjee, J. L. de Ris, Large eddy simulation of fire plumes, Proc. Combust. Inst. 33 (2011) 2473–2480.

[15] FM Global, FireFOAM, v1912, https://github.com/fireFoam-dev/, 2022.

[16] K. B. McGrattan, H. R. Baum, R. G. Rehm, A. Hamins, G. P. Forney, Fire Dynamics Simulator: Technical Reference Guide, Technical Report NISTIR 6467, National Institute of Standards and Technology, Building and Fire Research Laboratory, 2000. doi:10.6028/NIST.IR.6467.

[17] C. Lautenberger, C. Fernandez-Pello, Generalized pyrolysis model for combustible solids, Fire Safety J. 44 (2009) 819–839.

[18] J. Yang, H. Chen, N. Liu, Modeling of two-dimensional natural downward smoldering of peat, Energ. Fuel. 30 (2016) 8765–8775.

[19] C. Lautenberger, Gpyro3D: A three dimensional generalized pyrolysis model, Fire Safety Sci. 11 (2014) 193–207.

[20] X. Huang, G. Rein, Smouldering combustion of peat in wildfires: Inverse modelling of the drying and the thermal and oxidative decomposition kinetics, Combust. Flame 161 (2014) 1633–1644.

[21] X. Huang, G. Rein, H. Chen, Computational smoldering combustion:

Predicting the roles of moisture and inert contents in peat wildfires, Proc. Combust. Inst. 35 (2015) 2673–2681.

[22] X. Huang, G. Rein, Computational study of critical moisture and depth of burn in peat fires, Int. J. Wildland Fire 24 (2015) 798–808.

[23] X. Huang, G. Rein, Downward spread of smouldering peat fire: the role of moisture, density and oxygen supply, Int. J. Wildland Fire 26 (2017) 907–918.

[24] X. Huang, G. Rein, Upward-and-downward spread of smoldering peat fire, Proc. Combust. Inst. 37 (2019) 4025–4033.

[25] T. C. Mulky, K. E. Niemeyer, Computational study of the effects of density, fuel content, and moisture content on smoldering propagation of cellulose and hemicellulose mixtures, Proc. Combust. Inst. 37 (2019) 4091–4098.

[26] W. J. Jayasuriya, T. C. Mulky, K. E. Niemeyer, Smouldering combustion in cellulose and hemicellulose mixtures: Examining the roles of density, fuel composition, oxygen concentration, and moisture content, Combust. Theor. Model. 26 (2022) 831–855.

[27] E. Ranzi, A. Cuoci, T. Faravelli, A. Frassoldati, G. Migliavacca, S. Pierucci, S. Sommariva, Chemical kinetics of biomass pyrolysis, Energ. Fuel. 22 (2008) 4292–4300.

[28] G. Gentile, P. E. A. Debiagi, A. Cuoci, A. Frassoldati, E. Ranzi, T. Faravelli, A computational framework for the pyrolysis of anisotropic biomass particles, Chem. Eng. J. 321 (2017) 458–473.

[29] P. Reszka, P. Borowiec, T. Steinhaus, J. Torero, A methodology for the estimation of ignition delay times in forest fire modelling, Combust. Flame 159 (2012) 3652–3657.

[30] M. Kaviany, Principles of Heat Transfer in Porous Media, Springer Science & Business Media, 2012.

[31] S. Gordon, B. J. McBride, Computer program for calculation of complex chemical equilibrium compositions, rocket performance, incident and reflected shocks, and Chapman–Jouguet detonations, Technical Report NASA SP-273, National Aeronautics and Space Administration, 1976. URL: https://ntrs.nasa.gov/citations/19780009781.

[32] J. Blondeau, H. Jeanmart, Biomass pyrolysis at high temperatures: Prediction of gaseous species yields from an anisotropic particle, Biomass Bioenerg. 41 (2012) 107–121.

[33] M. W. Chase Jr, NIST-JANAF Themochemical Tables, volume 9 of *J. Phys. Chem. Ref. Data*, fourth ed., American Institute of Physics, 1998.

[34] R. B. Bird, W. E. Stewart, E. N. Lightfoot, Transport Phenomena, John Wiley & Sons, 1960.

[35] S. R. Turns, An Introduction to Combustion, McGraw-Hill, New York, 1996.

[36] L. F. Shampine, M. W. Reichelt, The MATLAB ODE suite, SIAM J. Sci. Comput. 18 (1997) 1–22.

[37] G. I. Marchuk, Some application of splitting-up methods to the solution of mathematical physics problems, Aplikace Matematiky 13 (1968) 103–132.

[38] E. S. Oran, J. P. Boris, J. P. Boris, Numerical Simulation of Reactive Flow, volume 2, Citeseer, 2001.

[39] G. Strang, On the construction and comparison of difference schemes, SIAM J. Numer. Anal. 5 (1968) 506–517.

[40] D. G. Goodwin, R. L. Speth, H. K. Moffat, B. W. Weber, Cantera: An object-oriented software toolkit for chemical kinetics, thermodynamics, and transport processes, https://www.cantera.org, 2021. doi:10.5281/zenodo.4527812, version 2.5.1.

[41] D. Behnoudfar, `ignm` [software], 2024. URL: https://github.com/dbehnoud/ignm. doi:10.5281/zenodo.10995085, commit `c51e18b`.

[42] T. Kashiwagi, T. Ohlemiller, K. Werner, Effects of external radiant flux and ambient oxygen concentration on nonflaming gasification rates and evolved products of white pine, Combust. Flame 69 (1987) 331–345.

[43] M. L. Ramadhan, J. Carrascal, A. Osorio, J. P. Hidalgo, The effect of moisture content and thermal behaviour on the ignition of eucalyptus saligna leaves, Int. J. Wildland Fire (2021).

[44] S. Matthews, A process-based model of fine fuel moisture, Int. J. Wildland Fire 15 (2006) 155–168.

[45] C. Anand, B. Shotorban, S. Mahalingam, S. McAllister, D. Weise, Physics-based modeling of live wildland fuel ignition experiments in the forced ignition and flame spread test apparatus, Combust. Sci. Technol. 189 (2017) 1551–1570.

[46] D. Behnoudfar, K. E. Niemeyer, Data, plotting scripts, and figures for "A physics-based ignition model with detailed chemical kinetics for live fuel burning studies" [dataset], Zenodo, 2024. doi:10.5281/zenodo.10982442.

Supplementary Material to "A physics-based ignition model with detailed chemical kinetics for live fuel burning studies"

Diba Behnoudfar[1] and Kyle E. Niemeyer[1]

[1]School of Mechanical, Industrial, and Manufacturing Engineering, Oregon State University

1 Discretization

This section provides the discretization schemes used for the numerical solution.

Equation (10):

$$\frac{\mathrm{d}}{\mathrm{d}t}\left(\bar{\rho}_g\phi\right)_n = -\left[\frac{\left(\dot{m}''\right)_{n+\frac{1}{2}} - \left(\dot{m}''\right)_{n-\frac{1}{2}}}{\Delta z}\right] + \sum\left(\dot{\omega}_j'''\right)_n \tag{1}$$

Equation (11):

$$\begin{aligned}\frac{\mathrm{d}}{\mathrm{d}t}\left(\bar{\rho}_g\phi Y_j\right)_n = &\left[\frac{\left(\dot{m}''\right)_{n+\frac{1}{2}}(Y_j)_n - \left(\dot{m}''\right)_{n-\frac{1}{2}}(Y_j)_{n-1}}{\Delta z}\right] \\ &+ \frac{\left(\bar{\rho}_g\phi\right)_n D_{n+\frac{1}{2}}\dfrac{(Y_j)_{n+1}-(Y_j)_n}{\Delta z} - \left(\bar{\rho}_g\phi\right)_{n-1} D_{n-\frac{1}{2}}\dfrac{(Y_j)_n-(Y_j)_{n-1}}{\Delta z}}{\Delta z} \\ &+ \left(\dot{\omega}_j'''\right)_n \end{aligned} \tag{2}$$

$$J_{(n+1/2,j)} = \left(\bar{\rho}_g\phi\right)_n D_{n+\frac{1}{2}}\frac{(Y_j)_{n+1}-(Y_j)_n}{\Delta z} \tag{3}$$

$$\left(\dot{m}''\right)_{n+1/2} = \frac{-K}{D_n}\frac{P_{n+1}-P_n}{\Delta z} - \frac{\left(\bar{\rho}_g\phi\right)_n}{\phi_n}g \tag{4}$$

$$D_{n+1/2} = \frac{D_{n+1}D_n}{D_{n+1} + (D_n - D_{n+1})/2} \tag{5}$$

Equation (15):

$$\begin{aligned}\frac{\mathrm{d}}{\mathrm{d}t}\left(\rho c_p T\right)_n = &-\dot{m}''\left[\frac{\left(c_pT\right)_n - \left(c_pT\right)_{n-1}}{\Delta z}\right] \\ &+ \rho\left[\frac{\left(Dc_p\right)_{n+1/2}\dfrac{T_{sur}-T_n}{\Delta x} - \left(Dc_p\right)_{n-1/2}\dfrac{T_n-T_{sur}}{\Delta x}}{\Delta x}\right] \\ &- \sum\left(\dot{\omega}_j'''h_j\right)_n \end{aligned} \tag{6}$$

Equation (16):

$$\frac{\mathrm{d}}{\mathrm{d}t}\left(\rho Y_j\right)_n = -\dot{m}''\frac{(Y_j)_n - (Y_j)_{n-1}}{\Delta z} + \rho\left[\frac{D_{n+1/2}\dfrac{(Y_j)_{sur} - (Y_j)_n}{\Delta x} - D_{n-1/2}\dfrac{(Y_j)_{sur} - (Y_j)_n}{\Delta x}}{\Delta x}\right] + \left(\dot{\omega}_j'''\right)_n \tag{7}$$

2 Algorithm

This section provides an example pseudocode describing how functions `ODE-func1` and `ODE-func2` are called at each time step to calculate the right-hand-side of Eqs. (10) and (11):

for all time steps:

- **solve** for Y_i , T, $\dot{\omega}_j'''$ using ODE solver and `ODE-func1`
- **solve** for $\bar{\rho_g}\phi$, $\bar{\rho_g}\phi Y_j$ using ODE solver and `ODE-func2`
  - **call** `ODE-func2`
    - **input** vectors of $[\bar{\rho_g}\phi]^{(t-1)}$, $[\bar{\rho_g}\phi Y_j]^{(t-1)}$, $[Y_i]^{(t-1)}$, $[T]^{(t-1)}$, $[\dot{\omega}_j''']^{(t-1)}$
    - **for** $n = 1$ to N (grid size)
      - $\phi_n = f(Y_i)$
      - $P_n = \dfrac{(\bar{\rho_g}\phi)_n}{\phi_n} \times R \times T_n$
      - $D_n = f(T_n, P_n)$
    - **for** $n = 1$ to $N - 1$
      - compute D
      - compute $(\dot{m}'')_n$
      - **if** $(\dot{m}'')_n < 0$ **then** $(\dot{m}'')_n = 0$
      - compute $J_{(n,j)}$ **for** $j = 1$ to gsp (# of gas species)
    - $(\dot{m}'')_N = \dfrac{-K}{D_N}\dfrac{P_0 - P_{N-1}}{\Delta z} - \dfrac{(\bar{\rho_g}\phi)_N}{\phi_N}g$ (at $z = 0$)
    - **if** $(\dot{m}'')_N < 0$
      - $(\dot{m}'')_N = 0$
    - $\dot{m}_1'' = J_{(1,j)} = 0$ (at $z = -H$)
    - $J_{(N,j)} = h_m(Y_j^{\infty} - (Y_j)_N)$ (at top boundary)
    - **if** $J_{(N,j)} < 0$
      - $J_{(N,j)} = 0$
    - **for** $n = 1$ to N
      - evaluate $\frac{\mathrm{d}}{\mathrm{d}t}\left(\bar{\rho_g}\phi Y_j\right)_n$ and $\frac{\mathrm{d}}{\mathrm{d}t}\left(\bar{\rho_g}\phi\right)_n$